Title	Three-dimensional finite element modelling for additive manufacturing of Ti-6Al-4V components: Effect of scanning strategies on temperature history and residual stress
Author(s)	Zhou, Jinbiao; Barrett, Richard A.; Leen, Sean B.
Publication Date	2022-03-22
Publication Information	Zhou, Jinbiao, Barrett, Richard A., & Leen, Sean B. (2022). Three-dimensional finite element modelling for additive manufacturing of Ti-6Al-4V components: Effect of scanning strategies on temperature history and residual stress. Journal of Advanced Joining Processes, 5, 100106. doi: https://doi.org/10.1016/j.jajp.2022.100106
Publisher	Elsevier
Link to publisher's version	https://doi.org/10.1016/j.jajp.2022.100106
Item record	http://hdl.handle.net/10379/17845
DOI	http://dx.doi.org/10.1016/j.jajp.2022.100106

Three-dimensional finite element modelling for additive manufacturing of Ti-6Al-4V components: effect of scanning strategies on temperature history and residual stress

Jinbiao Zhou[1,2,3], Richard A. Barrett[1,2,3], Sean B. Leen[1,2,3]

[1]Mechanical Engineering, College of Engineering and Informatics, NUI Galway.

[2]Ryan Institute for Environmental, Marine and Energy Research, NUI Galway.

[3]I-Form Advanced Manufacturing Research Centre, Ireland.

Abstract

A key challenge for metal additive manufacturing is the requirement to adapt process-structure-property methods currently under development to realistic, complex geometries. Of specific concern in the present work is the requirement for accurate computation in such realistic geometries of (i) thermal histories, to facilitate microstructure prediction, and hence, mechanical properties, and (ii) residual stresses, as required for accurate assessment and design for structural integrity, such as fatigue cracking. This paper presents three-dimensional, finite element modelling for simulation of a realistic Ti-6Al-4V component using directed energy deposition. The predicted results are successfully validated against published experimental and numerical data. The effects of different scanning strategies on temperature histories and residual stresses are investigated as a basis for identification of optimal manufacturing protocols. Finally, fatigue life predictions of the Ti-6Al-4V component have been considered based on the Basquin-Goodman equation with the effect of residual stress taken into account.

Keywords: Additive manufacturing; Directed energy deposition; Finite element analysis; Scanning strategies; Residual stress

1. Introduction

Additive manufacturing (AM) provides an unprecedented opportunity to produce complex metal parts through layer-by-layer addition of materials and offers a number of advantages over traditional manufacturing methods, including (i) ability to convert directly from three-dimensional computer solid models to near net-shape manufactured components in a single step, (ii) ability to manufacture features not typically achievable with conventional manufacturing, e.g. re-entrant corners and features, (iii) minimal waste of raw material

(powder), and (iv) possibility for recycling of powder, leading to reduced time to market via acceleratied prototyping and component or product customization at low cost [1]. AM processes can be generally classified into two main categories: (i) directed energy deposition (DED) (Fig. 1 (a)), in which the metal powder is fed coaxially into the beam and fuses with previously deposited thin layer, and (ii) powder bed fusion (PBF) (Fig. 1 (b)), in which a thin layer of powder is laid and then the metal powder is melted by the laser beam or electron beam according to a controlled trajectory [2, 3]. More details of AM technologies can be found elsewhere [4-6]. In this research work, the focus is mainly on laser directed energy deposition process. DED is able to manufacture and repair metal parts with high-performance and low-cost. Compared with conventional subtractive manufacturing methods, DED has unique advantages, especially in the manufacture of complex-shaped multi-materials or functionally graded components [7].

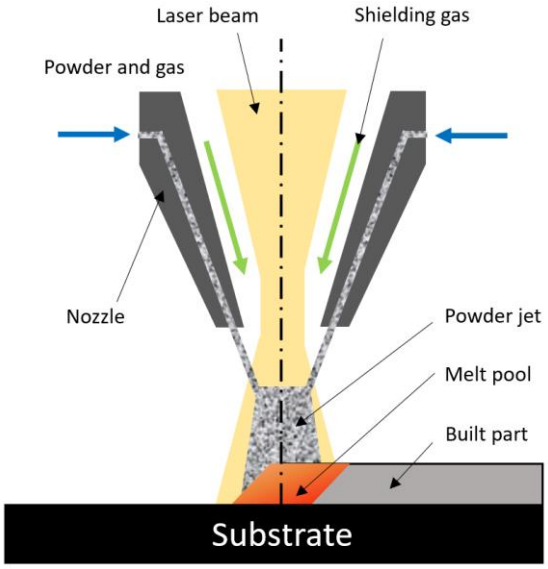

(a)

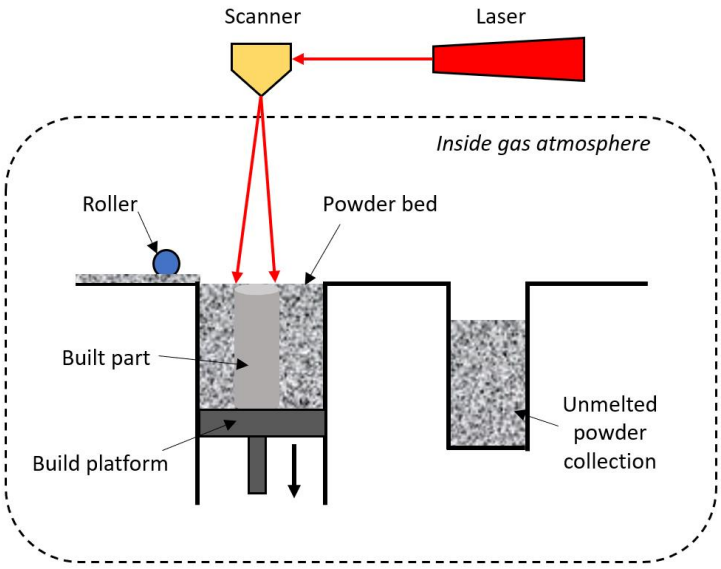

(b)

Fig. 1. Schematic illustrations of AM processes: (a) Directed Energy Deposition (DED) and (b) Powder Bed Fusion (PBF), adapted from Song et al. [8].

Although the advantages of AM are widely recognized, the residual stresses induced by the high and non-uniform thermal gradients during the laser heating and cooling cycles in the AM process is one of the major issues [9]. Residual stresses have a detrimental effect on mechanical strength and geometrical accuracy, particularly on fatigue resistance [10-12]. Hence, it is important to investigate and quantify the effects of manufacturing process on residual stresses, and resulting properties, e.g. fatigue life, for both the AM process and final AM components.

Finite element (FE) modelling of the AM process is a potentially powerful technique for full-field quantification of temporal-spatial distributions of key thermo-mechanical variables (e.g. temperature, deformation, strain, stress) directly or indirectly controlling the mechanical behavior of fabricated components. Several numerical models have been developed previously to simulate the AM process, with a focus on predicting thermal history and residual stresses and deformations. Zaeh et al. [13] presented a layer-by-layer modelling method to evaluate and quantify residual stress and deformation in relatively simple macro-scale components manufactured using the selective laser melting (SLM) process and highlighted the limitations of the layer-by-layer approach for predicting residual deformations. Barrett et al. [14] proposed a 2D layer-by-layer FE model to predict residual stress in PBF manufactured Ti-6Al-4V hip stem component (using a simplified 2D geometrical representation), highlighting the

importance of post-build heat treatment, but without explicit comparisons against experimental test data. Recently, an automated Python-based method for sectioning of 2D FE models of macroscale components for efficient model generation in the layer-by-layer method was developed [15], providing a framework for layer scaling for FE modelling of the PBF process. However, this method was not compared with test data for temperature histories or residual stresses. The layer-by-layer FE-based method was investigated for residual stress prediction of 3D PBF parts by Chen et al. [16], with a particular focus on geometrical shape (e.g. tri-prism, cylinder, block), solid and hollow. However, a key limitation of the layer-by-layer method is the inability to represent laser beam moving path and, hence, to investigate the effects of different scanning strategies, for example. The importance of scanning strategy (linear, zigzag, chessboard and contour) on residual deformation and surface finish in DED was demonstrated experimentally by Ribeiro et al. [17]. The contour strategy showed least distortion and best surface finish. The influence of scanning strategy on porosity, hardness and mechanical properties of Al2319 block structure were investigated by Matthieu et al [18]. The oscillation strategy showed comparable average percentage area porosity, hardness, UTS and YS to those reported in the literature. A common approach for simulating AM processes, including welding and 3D printing, is the significantly computationally-intensive 'element birth and death' method, also commonly referred to as the 'Model Change' method. This method is limited to small-scale geometries, e.g. low numbers of layers or tracks. Yang et al. [19] recently presented a 3D thermo-elastic-plastic model using this approach to follow precisely the physical deposition path for a 5-layer DED of Ti-6Al-4V. However, the high computational cost of these methods makes AM modelling of full scale and complex 3D components almost impossible. Chiumenti et al. [20] conducted a systematic assessment of different FE modelling techniques (e.g. layer-by-layer, hatch-by-hatch, element-by-element) for PBF, in terms of computational cost and numerical accuracy, particularly focusing on temperature prediction. Again, it recommended that the 'element birth and death' (high fidelity) method can be used for effects of different scanning strategies. Yang et al. [21] developed a FE model with a moving heat flux implemented via a user subroutine to predict the thermal history and spatial distributions of temperature of the PBF process and a process-structure model which can be used as a process design tool. In this case, the focus was on validation of temperature history against experimental measurement from the single-track PBF of Ti-6Al-4V, for prediction of phase transformations using a Kolmogorov-Johnson-Mehl-Avrami (KJMA) model. The process-structure method successfully predicted alpha and beta phase fractions. A key objective of the

present work is to adapt this process-structure method for realistic, large-scale components; however, the conventional 'Model Change' technique, e.g. in Abaqus [19, 21], is too computationally-expensive for such components. Recently, a new highly-efficient AM module has been developed within the general-purpose FE-based software Abaqus, which, on the one hand, replicates the actual 3D printing process very realistically and with high fidelity, e.g. using actual 3D printing stereolithography (STL) files, whilst, on the other hand, providing a much more efficient process for modelling complex geometries, including a graphical user interface (GUI) [22]. This approach, which is the main method investigated in this paper, is hereafter referred to simply as 'Abaqus AM', and has recently been evaluated by Song et al. [8] for AM (laser DED and PBF) of complex, three-dimensional Inconel 718 components; the results were compared to experimental measurements of residual stresses and distortions, the latter obtained using (i) a combined focused ion beam (FIB) slitting, and digital image correlation (DIC) method and (ii) X-ray diffraction (XRD), at different length-scales. The predicted residual distortions were reasonably accurate in general whereas predicted residual stresses compared favorably for some components and not so favorably for others. It was concluded that (i) further work is required on the effects of measured plastic anisotropy on as-built properties [23] and (ii) future research needs to focus on more accurate measurements of these critical material properties at elevated temperature to improve process simulation accuracy. A similar modelling approach by Yang et al. [24] achieved high accuracy compared to experimental measurements for predicting residual strains in PBF of Inconel 625. Apart from the residual stress prediction, it is also important to investigate the effect of residual stress on fatigue life of components with complex geometry. Jiang et al. [25] evaluated the role of residual stress on fatigue life of 316L stainless steel; the results showed that the tensile residual stress caused increase of mean stress and, hence, decrease of the fatigue life. Devaney et al. [26] applied a Basquin-Goodman methodology relating fatigue life to stress range and mean stress [27] to estimate the fatigue life at different locations in a complex welded X100 steel catenary riser connection; the results showed superior performance of the X100 material compared to more conventional X70 steels for example.

This paper presents three-dimensional, finite element modelling for prediction of temperature-time histories and residual stress distributions of a realistic (macro-scale) Ti-6Al-4V component manufactured using DED. A comparative assessment is presented, initially, between the (highly efficient but less accurate) layer-by-layer FE-based method and the new (efficient and high accuracy) 'Abaqus AM' method, in terms of temperature-time histories

against (i) previously-published 'Model Change' results [19, 21] and (ii) measured cooling rates. The latter are key for metallurgical transformations [21], and hence, as-built mechanical property prediction. A more detailed validation of the new Abaqus-based modelling method is then presented by way of comparison against published thermocouple data from a DED process of the three-dimensional component. The accuracy and efficiency of the new Abaqus-based method is verified by comparison to previously-published numerical results for residual stress prediction. A study on the effects of scanning strategy on three-dimensional temperature and residual stress distributions is presented, as a basis for identification of optimal manufacturing protocols and to demonstrate the effectiveness of the proposed modelling method. Finally, some sample fatigue life calculations are presented using a combined Basquin-Goodman approach, to demonstrate typical effects of the predicted AM-induced residual stresses for sample locations in the manufactured component, including the effect of scanning strategy, followed by some discussions and conclusions. Attention is focused here on uniaxial high cycle fatigue behavior for long life of components; hence the Basquin model is adopted, due to its simplicity and widespread use [Fuchs, Stephens and Stephens; Suresh]; the Goodman equation is widely used to incorporate the effects of mean stress on high cycle fatigue, and is therefore also adopted here to assess effects of residual stresses on HCF life for the AM Ti6Al4V components.

2. Methodology

There are several physical phenomena to consider in the DED process, including the thermal transfer, moving heat source, and material deposition. The widely-used sequentially coupled thermal and mechanical FE analysis approach is adopted to describe the DED process accurately and efficiently [8, 24, 28-30]. 3D transient thermal analysis is performed first, and then the thermal loading from the heat transfer analysis are coupled to the same FE model for mechanical analysis.

2.1 Thermal mechanisms

2.1.1 Heat transfer equations

The main thermal mechanisms in DED are (i) conduction within the part, (ii) conduction between the part and substrate, and (iii) convection and radiation between the active layer and the surrounding air, as shown in Fig. 2. The governing equation for the heat transfer process is

written using the energy equation [31], as follows:

$$\rho \frac{dH(\mathbf{r},t)}{dt} = -\nabla \cdot \mathbf{q} + Q + \dot{D}_{\text{mech}} \tag{1}$$

where $\mathbf{r}$ represents an arbitrary reference material point in a Lagrangian domain Ω, ρ is material density (kg/m^3), H is enthalpy, t is time (s), $\mathbf{q}$ is heat flux vector, and Q is laser heat source, $\dot{D}_{\text{mech}}$ is thermo-mechanical dissipation. The temporal rate of enthalpy can be expressed as:

$$\frac{dH(\mathbf{r},t)}{dt} = C_{\text{p}}(T) \frac{dT(\mathbf{r},t)}{dt} \tag{2}$$

where C_{p} is the temperature dependent specific heat (J/kgK), T denotes temperature (K). The heat flux vector $\mathbf{q}$ is given by Fourier's law, as:

$$\mathbf{q} = -k(T)\nabla T \tag{3}$$

where k is temperature dependent thermal conductivity (W/mK), which, for simplification purposes, is assumed to be isotropic here [19, 32]. Of course, thermal conductivity may possibly be anisotropic due to the mechanisms of AM metal [refs]; future work will investigate this further. The thermo-mechanical dissipation $\dot{D}_{\text{mech}}$ is defined as [33]:

$$\dot{D}_{\text{mech}} = \boldsymbol{\sigma} : \dot{\boldsymbol{\varepsilon}}^{\text{vp}} \tag{4}$$

where $\boldsymbol{\sigma}$ is the stress tensor and $\dot{\boldsymbol{\varepsilon}}^{\text{vp}}$ is the visco-plastic strain tensor. The heat loss due to heat convection is given by Newton's law of cooling, as:

$$q_{\text{conv}} = h_{\text{conv}}(T_{\text{s}} - T_{\text{env}}) \tag{5}$$

where h_{conv} is heat transfer convection coefficient (W/m^{2}K), T_{s} is surface temperature of the specimen (K), T_{env} is environmental temperature (K). Here, a force convection coefficient $h_{\text{conv-force}} = 55$ W/m^{2}K was used during the printing process, while a free convection coefficient $h_{\text{conv-free}} = 5$ W/m^{2}K was applied as the reference [19, 34, 35] because the argon atmosphere is no longer available after the printing process and the convection becomes uniform on all surfaces. The heat loss due to heat radiation is defined by Stefan-Boltzmann's law:

$$q_{\mathrm{rad}} = \varepsilon_{\mathrm{rad}}\sigma_{\mathrm{rad}}(T_{\mathrm{s}}^4 - T_{\mathrm{env}}^4) \tag{6}$$

where $\varepsilon_{\mathrm{rad}}$ is the emissivity coefficient, and σ_{rad} is the Stefan–Boltzmann constant. Here, the emissivity was assumed to be temperature independent as 0.54 [34], and the Stefan-Boltzmann's constant was set as $5.669 \times 10^{-8}\ \mathrm{W/m^2K^4}$ [36, 37].

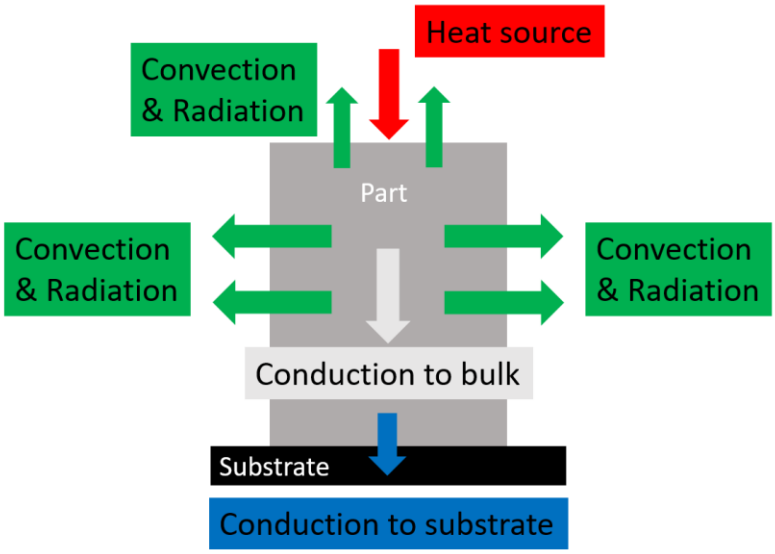

Fig. 2. Thermal transfer mechanisms during the DED process.

2.1.2 Heat source equations

The Goldak double ellipsoidal model, which has been widely adopted to describe the laser heat source Q in Eq. (1) during the DED process modelling [8, 32, 38-40], is employed in the present work, defined as:

$$\begin{gathered} Q = q_f \quad when\ x_1 \geq 0 \\ Q = q_r \quad when\ x_1 < 0 \\ q_{f/r} = \frac{6\sqrt{3} f_{f/r} A P}{abc\pi\sqrt{\pi}} e^{\left(-\frac{3x_1^2}{c_{f/r}^2} - \frac{3y_1^2}{a^2} - \frac{3z_1^2}{b^2}\right)} \end{gathered} \tag{7}$$

where f_f and f_r are 'box size' factors with a value of 1, A is the heat source absorption coefficient, P is the laser power (W) and x_1, y_1, z_1 are the local coordinates with origin centered on the moving heat source when the scanning speed v reaches the maximum value, a, b are the dimensions along the y_1 and z_1 axis of the ellipsoid and c_f and c_r are the front length and rear length along the x_1 axis of the ellipsoid, as shown in Fig. 3**.** Generally, a, c_f and c_r are taken

as the laser spot radius, b is taken as the melt pool depth [8, 19]**.** The inputs for the Goldak heat source model are based on the DED manufacturing parameters of the experimental conditions investigated here [19], as summarized in Table 1.

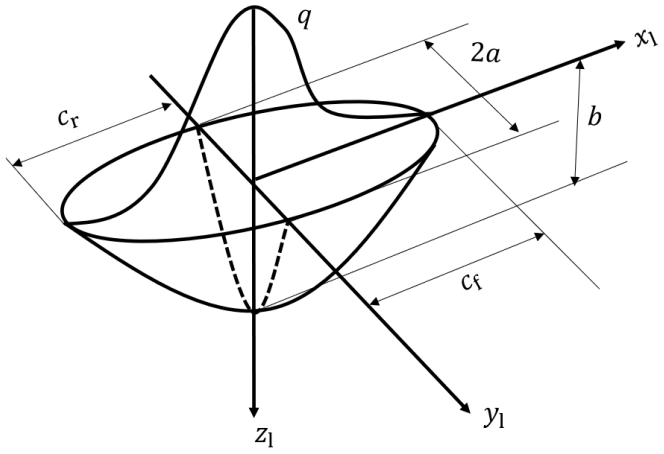

Fig. 3. The Goldak double ellipsoid heat source model for DED process.

Table 1. Printing process parameters applied.

Symbol	Parameters	Value
P	Laser power (W)	300
A	Heat source absorption coefficient	0.45
v	Laser scanning speed (mm/s)	2
R	Laser spot radius (mm)	1.36
d_{m}	Melt pool depth (mm)	0.816

2.2 Mechanical mechanisms

The momentum balance equation used for the mechanical analysis is given by [37, 41]:

$$\nabla \cdot \boldsymbol{\sigma} + \mathbf{b} = 0 \tag{8}$$

where $\boldsymbol{\sigma}$ is the Cauchy stress tensor and $\mathbf{b}$ is the body force. The mechanical constitutive law of the elastic problem is defined as:

$$\boldsymbol{\sigma} = \boldsymbol{C} : \boldsymbol{\varepsilon}_{\mathbf{e}} \tag{9}$$

where $\boldsymbol{C}$ is the fourth order elastic tensor and $\boldsymbol{\varepsilon}_{\mathbf{e}}$ is the elastic strain tensor, which is calculated by:

$$\boldsymbol{\varepsilon_e} = \boldsymbol{\varepsilon_{Total}} - \boldsymbol{\varepsilon_p} - \boldsymbol{\varepsilon_T} \quad (10)$$

where $\boldsymbol{\varepsilon_{Total}}$, $\boldsymbol{\varepsilon_p}$, $\boldsymbol{\varepsilon_T}$ are the total, the plastic and the thermal strains, respectively. The thermal strain is defined as:

$$\boldsymbol{\varepsilon_T} = \alpha \Delta T \boldsymbol{I} \quad (11)$$

where α is the thermal expansion coefficient (10^{-3}/K), ΔT is the change in temperature (℃) and $\boldsymbol{I}$ is identity tensor. The tensile testing on the AM Ti-6Al-4V, which is used in the experiment investigated here [19], shows extensive plastic deformation with limited work hardening [42]. Hence, the widely employed elastic perfectly plastic model is adopted to define the constitutive behaviour of material in this study [43, 44].

2.3 Additive manufacturing simulation techniques

2.3.1 Layer-by-layer method

The macroscale part is sectioned into microscale equivalent layers along the building direction for the layer-by-layer model (see Fig. 4), in which the whole layer is heated by an equivalent heat resource simultaneously, to save computational cost in AM modelling [14, 15, 45]. The equivalent heat source Q_{e} is defined based on the printing process parameters (see Table 1):

$$Q_{\mathrm{e}} = \frac{AP}{d_{\mathrm{s}} d_{\mathrm{m}} H} \quad (12)$$

where d_{s} is the laser spot radius (mm), d_{m} is the melt pool depth (mm) and H is the hatch spacing (mm), taken as laser spot diameter here. The heating time t_{heat} of each equivalent layer is calculated by:

$$t_{heat} = \frac{d_s}{v} \quad (13)$$

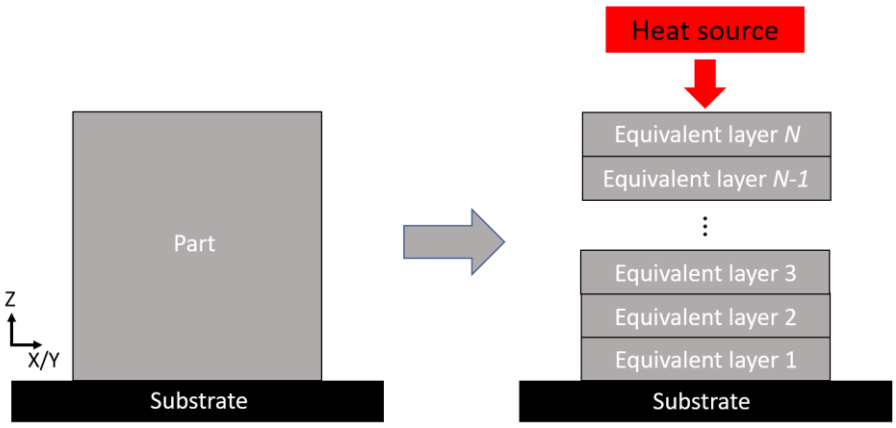

Fig. 4. The schematic diagram of the layer-by-layer method.

2.3.2 Present FE-based AM method (Abaqus AM module)

Historically, the 'Model Change' technique has been used to simulate the addition of new material with time. This is computationally inefficient for progressive material addition, and is limited to simple geometries [32]. As mentioned above, a new AM simulation module has recently been implemented within the general-purpose non-linear FE code, Abaqus [46]. This method is investigated here for simulation of the complete AM process for complex components. This implementation is significantly more efficient for (i) progressive element activation for modelling the deposition of materials and (ii) moving heat fluxes for modelling the laser heating process. The Event Series module is utilized to prescribe the combination of toolpath and process conditions which needs to be interpreted numerically both in time and space according to the element activation and related heat input. The newly introduced toolpath-mesh intersection module, which makes the model set-up simpler and less time-consuming, can then be used to calculate the relevant information required for the thermal and structural FE analysis automatically after defining the event series in input files [8]. This is used to determine which elements have intersected with a path that is defined in time and space, for example the path of a tool. Previous methods were limited to adding elements at the start of a step, and required explicit definition of the elements to be included [13, 19-21]. The toolpath-mesh intersection module allows for a much looser coupling between the toolpath and the rest of the model, giving simpler and faster model set-up. The overall approach, as illustrated in Fig. 5.

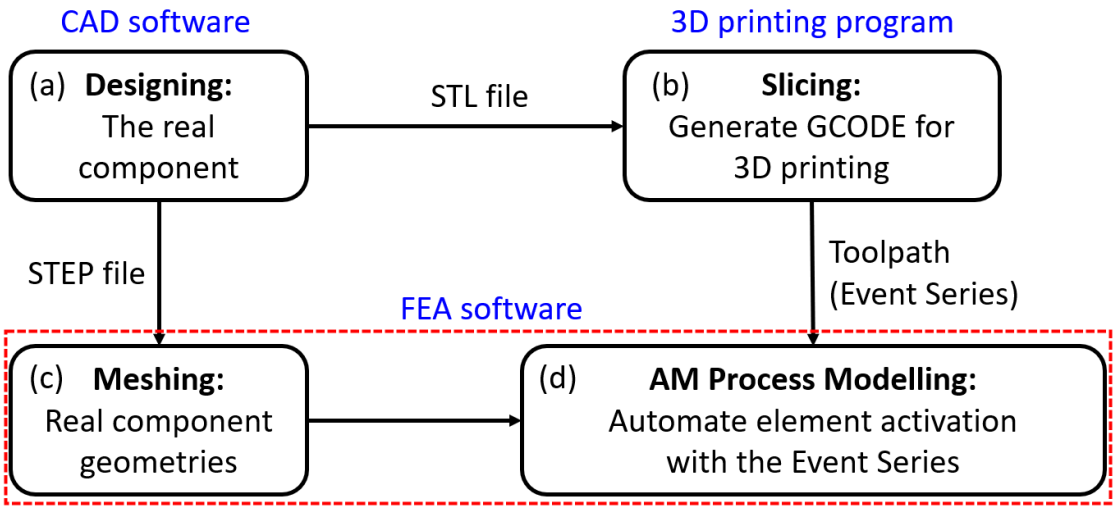

Fig. 5. Overall AM modelling flowchart: (a) step 1: Designing, (b) step 2: Slicing, (c) step 3: Meshing, (d) step 4: AM process modelling.

2.4 Rectangular model and material properties

A five-layer hollow rectangular-shaped specimen (long length 41.86 mm, short length 22.37 mm, height 4.43 mm, and width 2.72 mm) on a square substrate (width 101.6 mm and thickness 3.18 mm) is modelled corresponding to the experimental arrangement [19] using the 'Abaqus AM' method to simulate the DED process (Fig. 6 (a)). The layer height L_h is 0.886 mm. A detailed mesh convergence study is conducted to establish a suitable refined element size for the built part, with the final mesh (Fig. 6 (b)) using an element size (0.68 mm in x direction, four elements in width) based on the suggestions proposed in Refs [19, 32, 34], and converged to within 5% with respect to stress. The converged FE model contains 8562 elements and 13152 nodes. Eight-node linear heat transfer elements (DC3D8) and eight-node linear elements with full integration (C3D8) are chosen for the thermal and mechanical analysis, respectively [8]. For both thermal and mechanical analysis, the full element activation [24] is utilized to simulate the addition of material during the AM process.

The build direction for the hollow rectangular-shaped specimen is defined in the global z-direction (Fig. 6 (b)). Temperature-dependent material properties of Ti-6Al-4V are employed in this study as taken from [34], presented in Table 2. The material density and Poisson's ratio are assumed to be a constant of 4430 kg/m^3 and 0.34 respectively [19]. The initial temperature of the whole model is set to be an ambient temperature of 27 ^{o}C. The substrate, which is also made of Ti-6Al-4V, is clamped at the left side to match the experimental settings, as shown in Fig. 6 (b).

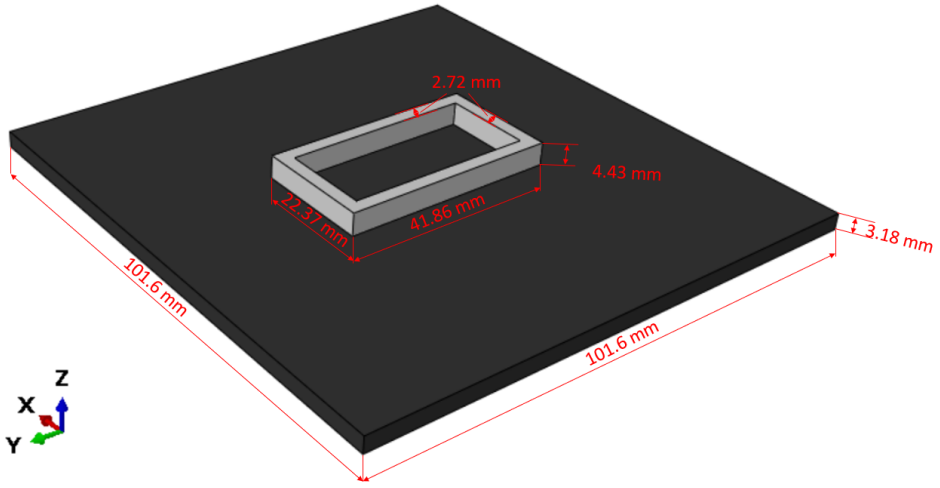

(a)

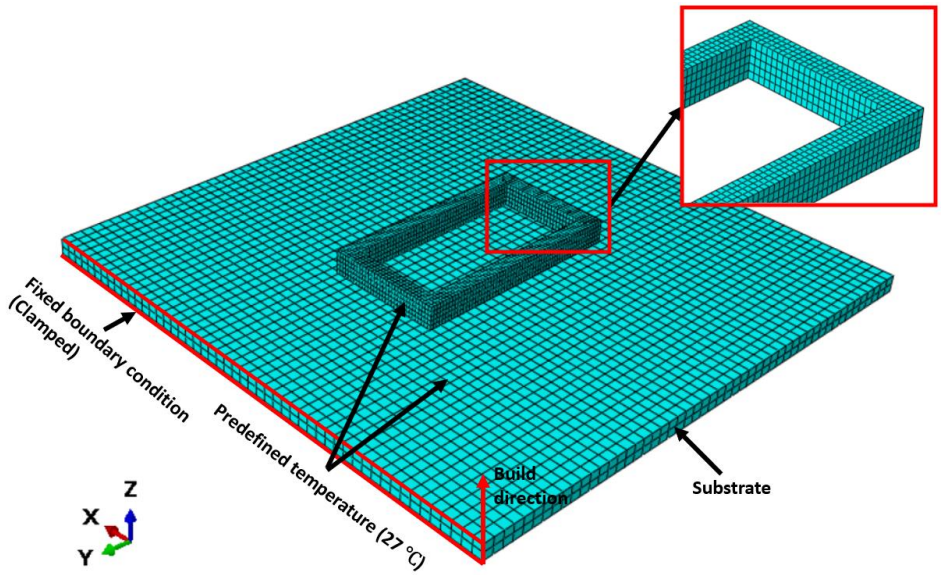

(b)

Fig. 6. Finite element model of substrate and part geometry for DED simulation (a) Model configurations, (b) Finite element mesh and boundary conditions.

Table 2. Temperature dependent material properties of Ti-6Al-4V [34].

Temperature T (°C)	**Specific heat C_p (J/kg/°C)**	**Conductivity k (W/m/°C)**	**Thermal expansion coefficient α (µ m/m/°C)**	**Elastic Modulus E (MPa)**	**Yield strength σ_y (MPa)**
20	565	6.6	8.64	103950	768.15
93	565	7.3	8.82	100100	735.3

205	574	9.1	9.09	94190	684.9
250	586	9.7	9.2	91810	664.65
315	603	10.6	9.33	88380	635.4
425	649	12.6	9.55	82580	585.9
500	682	13.9	9.7	78630	552.15
540	699	14.6	9.7	76520	534.15
650	770	17.5	9.7	70720	484.65

2.5 Scanning strategies

Three different scanning strategies are employed in the DED process modelling to investigate the effect on thermal distribution and resulted residual stress. These are denoted as strategies A [19], B [47], C, respectively, as shown in Fig. 7. '1', '2', '3', '4' are marked to represent the deposition sequence of the hollow rectangular-shaped specimen: green points and bold arrow lines represent the start and direction of each deposition layer. The maximum time that the deposited material has to cool before the new layer to be deposited for strategy A, B and C are 58.8 s, 78 s and 117.6 s, respectively. Different material deposition and moving heat event series are programmed to define the motion of powder and the laser moving path according to the respective scanning strategies.

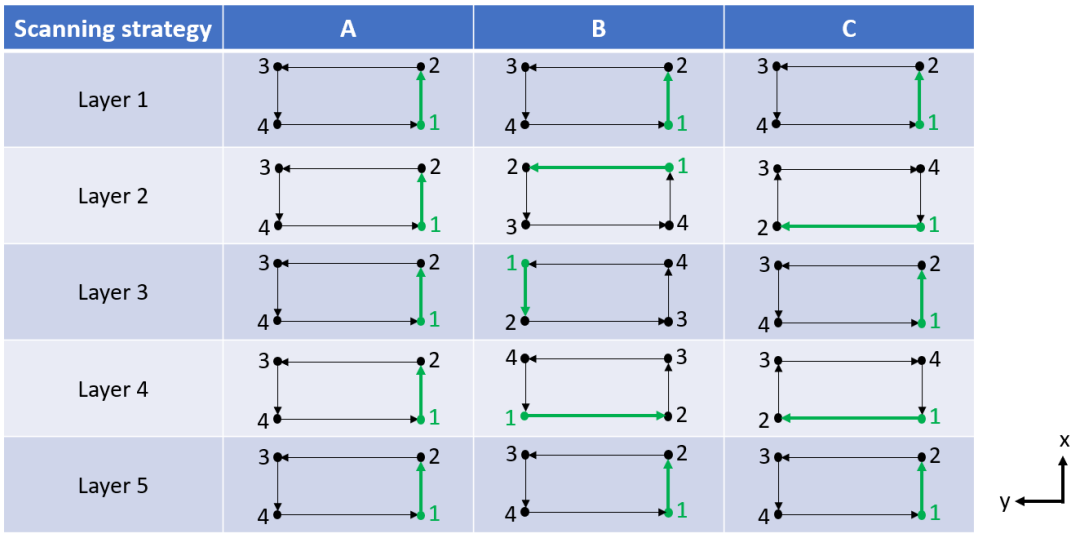

Fig. 7. Schematic diagram of different scanning strategies.

3. Results

3. 1 Verification and validation of AM simulation techniques

3.1.1 Verification of AM simulation techniques

In this present study, the DED process for Ti-6Al-4V specimens is investigated using both the layer-by-layer method and the 'Abaqus AM' method to verify the accuracy of the proposed AM modelling techniques via comparison to published results. Fig. 8 shows the position of a selected point (at the center of the first layer), which is 38.8 mm away from the laser start point (left corner of first layer). The comparison of the FE-predicted thermal history for the selected point by layer-by-layer modelling against the numerical results using the 'Model Change' technique reported by Baykasoglu et al. [32] for the same point is shown in Fig. 9. A similar temperature profile is predicted by the layer-by-layer method, however, a time difference is clearly shown between the time of peak temperature of the layer-by-layer method and that in Ref [32]. For example, the time of the first peak predicted by the layer-by-layer method is 1.36 s, while the first peak in the published result arrives at 19.4 s: the cause of the difference is that the whole layer is heated simultaneously using the layer-by-layer method, since the real laser travelling time has not been modelled. The first temperature peak (first layer deposition) in both methods is almost identical, approximately 1800 oC. However, subsequent peaks are significantly different in magnitude; e.g. the layer-by-layer method underpredicts the second peak by about 500 oC viz. 1200 oC compared to 1700 oC. These differences after the first layer are primarily attributed to longer cooling times in the layer-by-layer method. Furthermore, the sampled point for temperature is on the first layer, the distance between the new layer and the first layer increases with the deposition process, which makes the peak temperature measured from the first layer decreases gradually. Fig. 10 presents the FE-predicted thermal history at the same selected point using the 'Abaqus AM' method, corresponding to the deposition of five layers. This clearly shows five primary peaks in temperature, both the trend and peak temperature are in good agreement with the published numerical results [32]. The comparison of predicted and measured cooling rates is summarised in Table 3, including the measured result from DED Ti-6Al-4V experiment by Lia et al. [48, 49]. The FE-predicted cooling rate using the 'Abaqus AM' method is seen to be significantly closer to the test measurement than the prediction by Baykasoglu et al. [32]. It is important to note that for the case here using 8 CPUs, the total runtime for this model is around 4 hours for the thermal analysis, using the 'Abaqus AM' method, compared to approximately 6 times CPU time using the 'Model Change' technique.

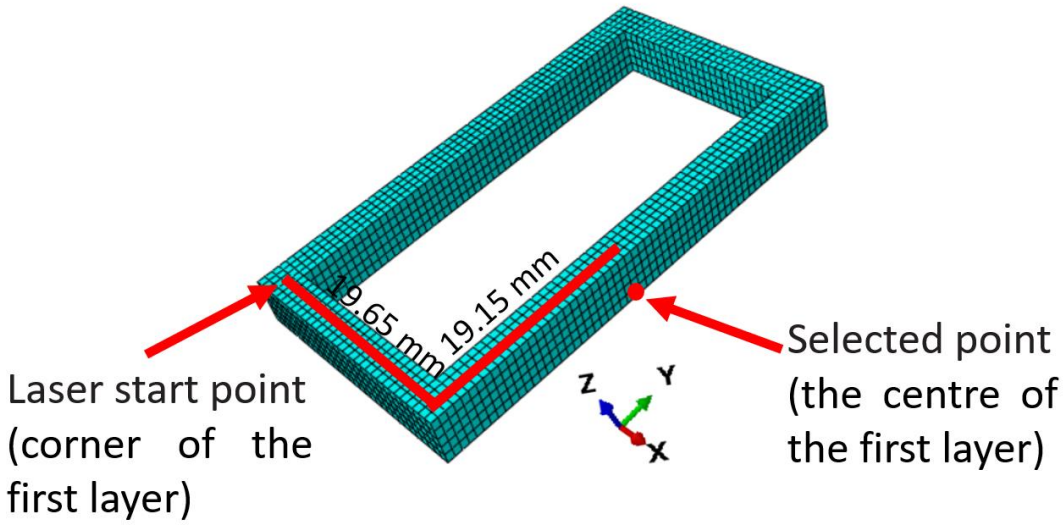

Fig. 8. Illustration of position of selected point (at the centre of the first layer).

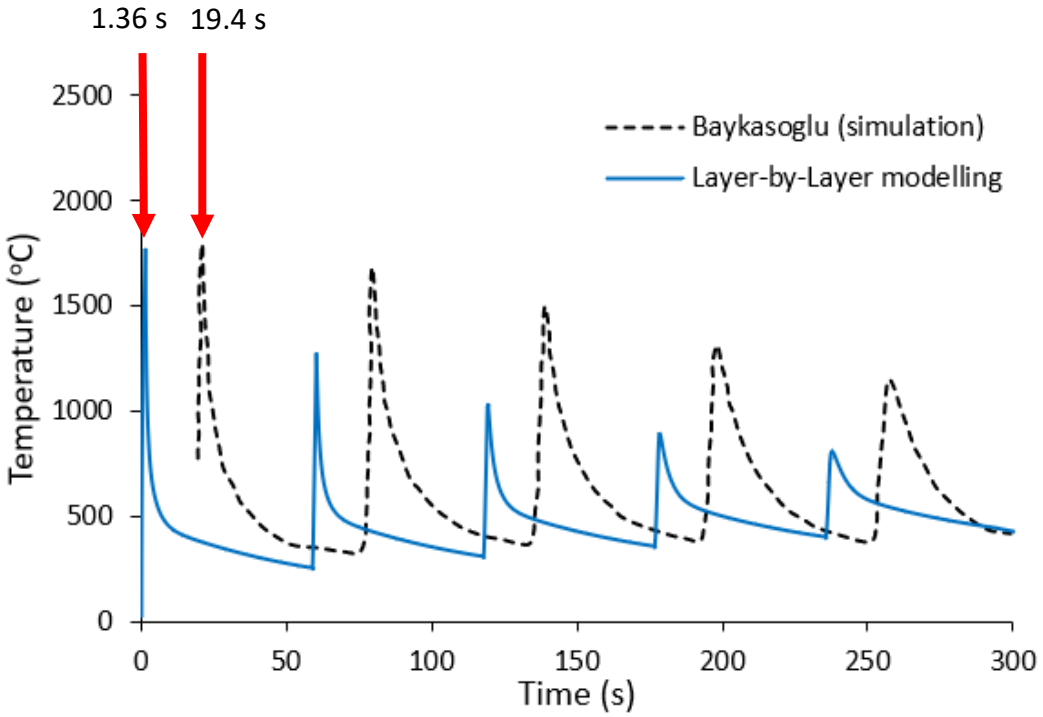

Fig. 9. Comparison of FE-predicted thermal history for selected point using the layer-by-layer method against independent numerical results from Baykasoglu et al. [32] using the more computationally-expensive 'Model Change' technique.

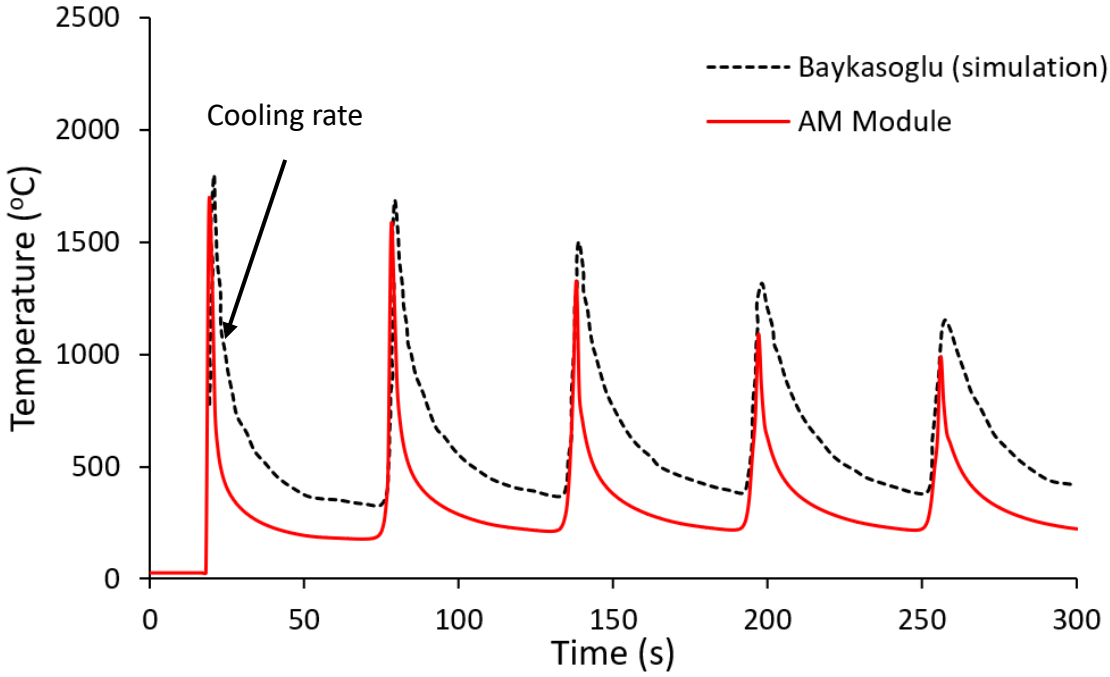

Fig. 10. Comparison of FE-predicted thermal history for selected point against independent numerical results from Baykasoglu et al. [32] using the more computationally-expensive 'Model Change' technique.

Table 3. Comparison of predicted and measured cooling rates of DED Ti-6Al-4V.

Source	Cooling rate (°C/s)
Simulation [32]	~ 100
Present work with 'Abaqus AM'	~ 200
Test [49]	219 ± 6.1

3.1.2 Validation of AM simulations

The FE thermal analysis results are validated by comparison to the experimental measurement results reported by Yang et al. [19], where the rectangular shaped Ti-6Al-4V specimen was produced using the Optomec LENS system [50], and two Omega SA1XL-K-72 thermocouples (TC) were attached on the top and bottom surfaces of the substrate to collect the temperature data during the heating (printing) and cooling processes. Time and temperature were recorded with 100 Hz sampling rate. The locations of the two TCs are shown in Fig. 11, where the solid black circle represents TC1 on the top surface of the substrate and the empty black circle represents TC2 on the bottom surface of the substrate.

The predicted temperature histories are obtained at the same TC locations as in the experimental measurements. Fig. 12 shows the temperature comparison between the predicted (using the layer-by-layer method and the AM Module method) and experimental measurements. It is clear from Fig. 12 that during the heating process (from 0 s to 293.9 s), the experimental results and the numerical results using the AM Module method follow a very similar trend, and their trends are almost the same during the cooling process (from 294 s to 1600 s), while the predictions using the Layer-by-Layer method are much higher than the experimental measurements, which may due to the whole layer is heated simultaneously during the Layer-by-Layer modelling. The comparison also validates the developed FE model through the thickness direction (z direction) (Fig. 11) as TC1 and TC2 are on the top and bottom surfaces of the substrate, respectively. Compared to TC1, the measured temperature at TC2 is higher, especially during the heating process, which is due to TC2 being 5 mm closer to the deposition part in the x direction (Fig. 11) than TC1.

The predicted temperature field distribution at the end of printing (before the start of the cooling process) is shown in Fig. 13: both the contour plot and maximum temperature (viz. 2432 ^{o}C, as compared to 2447 ^{o}C) are found to be comparable to the numerical results reported by Yang et al. [19]. The predicted contours of residual stress σ_{x} and σ_{y} along the x and y direction are shown in Fig. 14. Fig. 15 presents the comparison of predicted maximum of spatial residual stress. Regardless of maximum stress location or value, both σ_{x} and σ_{y} are in close agreement with the predictions from Yang et al. [19] using more computationally-expensive 'Model Change' technique.

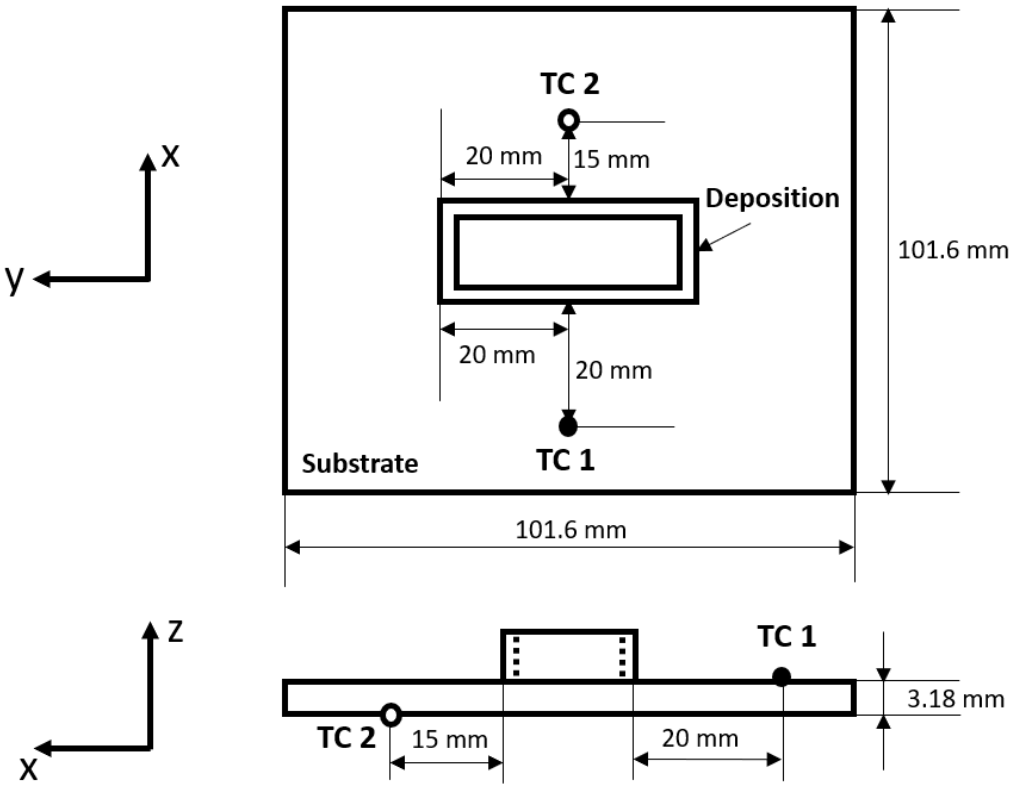

Fig. 11. Locations of the two thermocouples measurement points: TC1 (solid circle) on top surface and TC2 (empty circle) on bottom surface of the substrate.

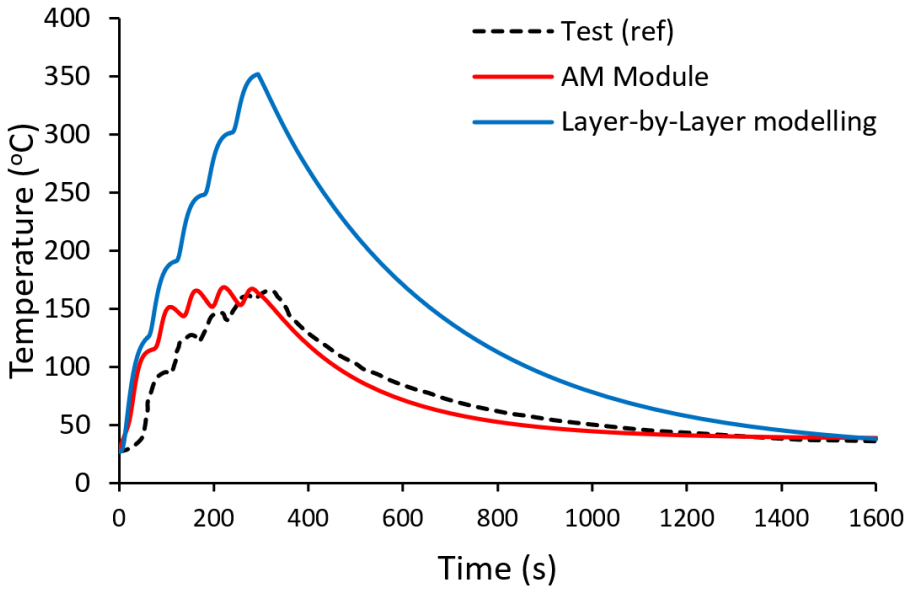

(a)

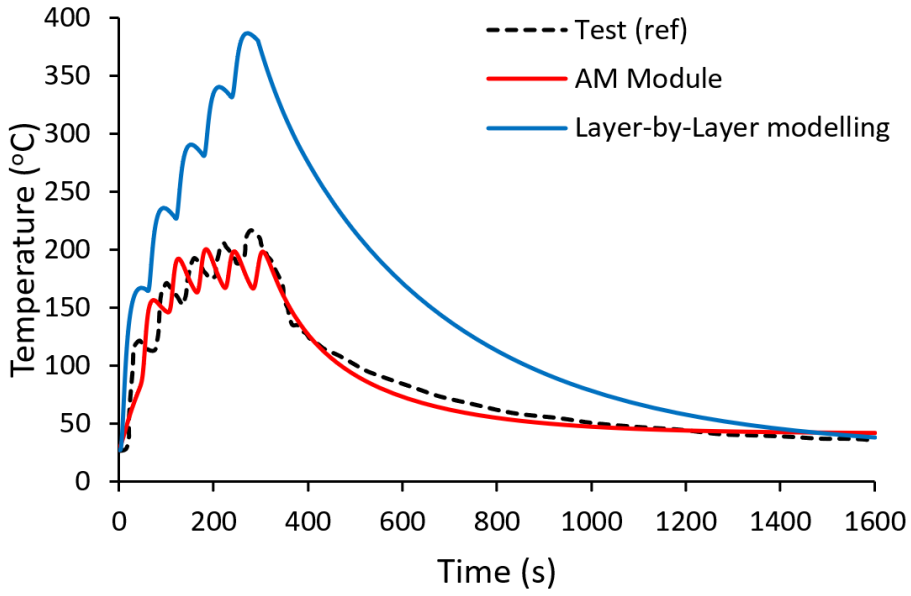

(b)

Fig. 12. Temperature history comparison between the predicted using the layer-by-layer method and the AM Module method and experimental measurements (Ref [19]) at (a) TC1 and (b) TC2.

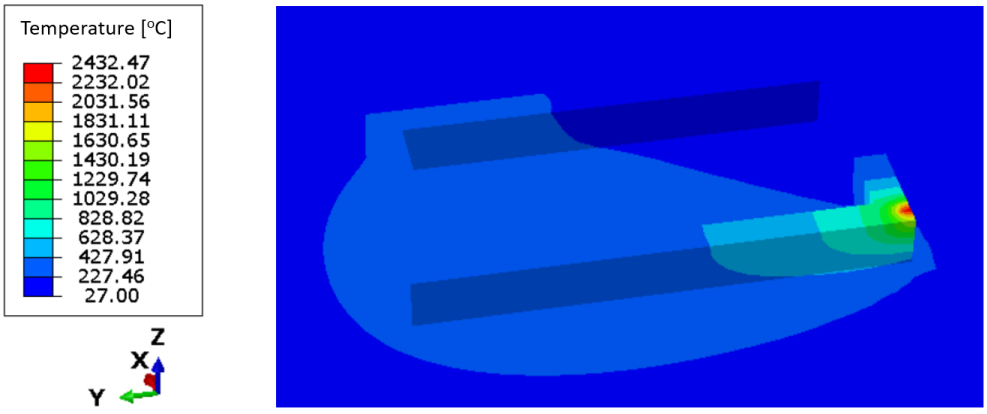

Fig. 13. The predicted temperature distribution with scanning strategy A (Fig. 7) at the end of the printing before cooling starts.

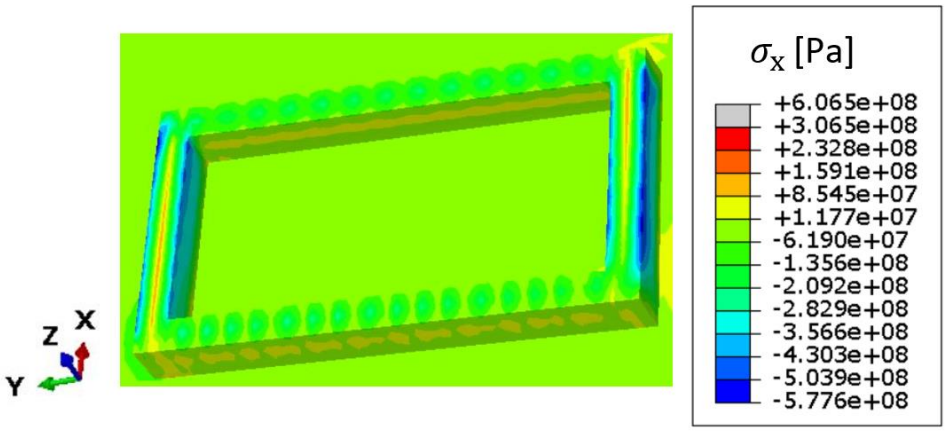

(a)

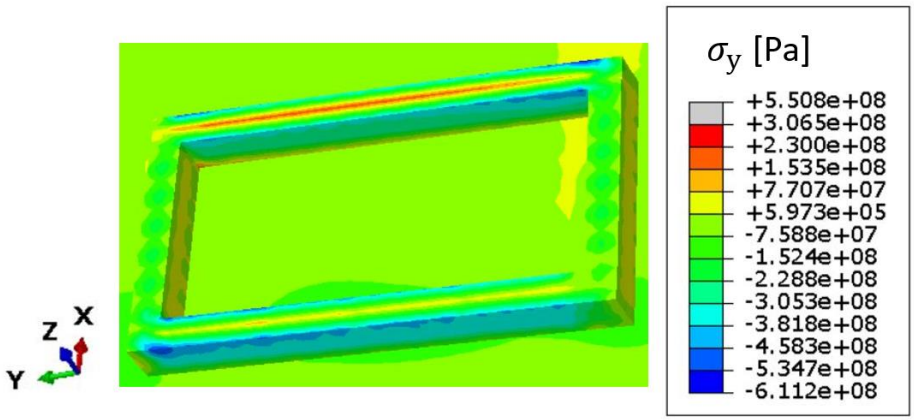

(b)

Fig. 14. The predicted stress distribution with scanning strategy A (Fig. 7): (a) σ_x: residual stress along the x direction and (b) σ_y: residual stress along the y direction.

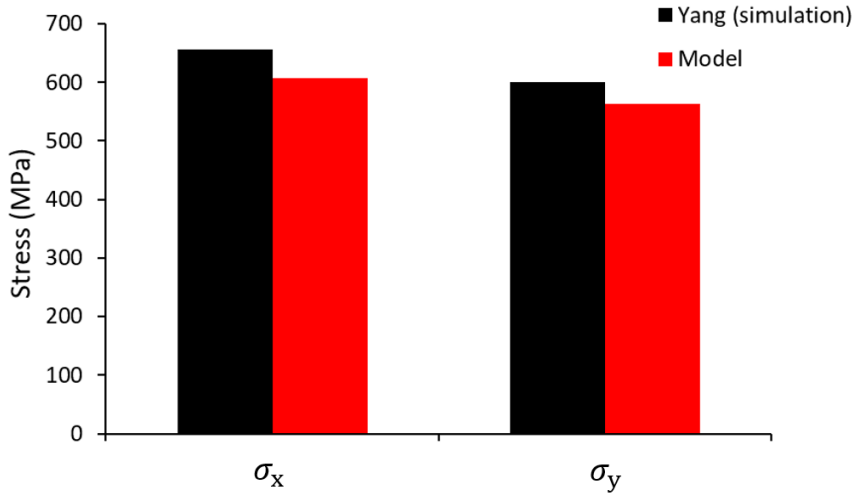

Fig. 15. The comparison of predicted maximum (spatial) residual stress.

3. 2 Thermal profile of different scanning strategies

To understand the influence of scanning strategy on the thermal profile, the temperature distributions at certain layers with the different scanning strategies are extracted. The laser scanning sequence is varied while the same laser heat source is employed for all scanning strategies. As a result, the thermal distributions are different based on the scanning strategy. The FE modelling results for the temperature contours with the same legend of the additively manufactured rectangular shaped Ti-6Al-4V specimen at the end of layer 4 with using various scanning strategies are demonstrated in Fig. 16. The maximum temperature at layer 4 of the rectangular specimen in relation to the respective scanning strategies is indicated by the text and arrow on each image in Fig. 16. It is clearly shown that both the value and location of maximum temperatures with each scanning strategy are different. Comparing all the scanning strategies, Strategy A (Fig. 7) exhibits the highest maximum temperature at the bottom of the long side of the specimen (2214 ^{o}C, Fig. 16 (a)), while Strategy C (Fig. 7) exhibits the lowest maximum temperature at the right short side of the specimen (2145 ^{o}C, Fig. 16 (c)). This may due to the changing direction between each layer providing longer cooling time for the specimen. Strategy B has a predicted maximum temperature on the left short side of the specimen (2148 ^{o}C, Fig. 16 (b)), where the start point is changed for each layer (Fig. 7).

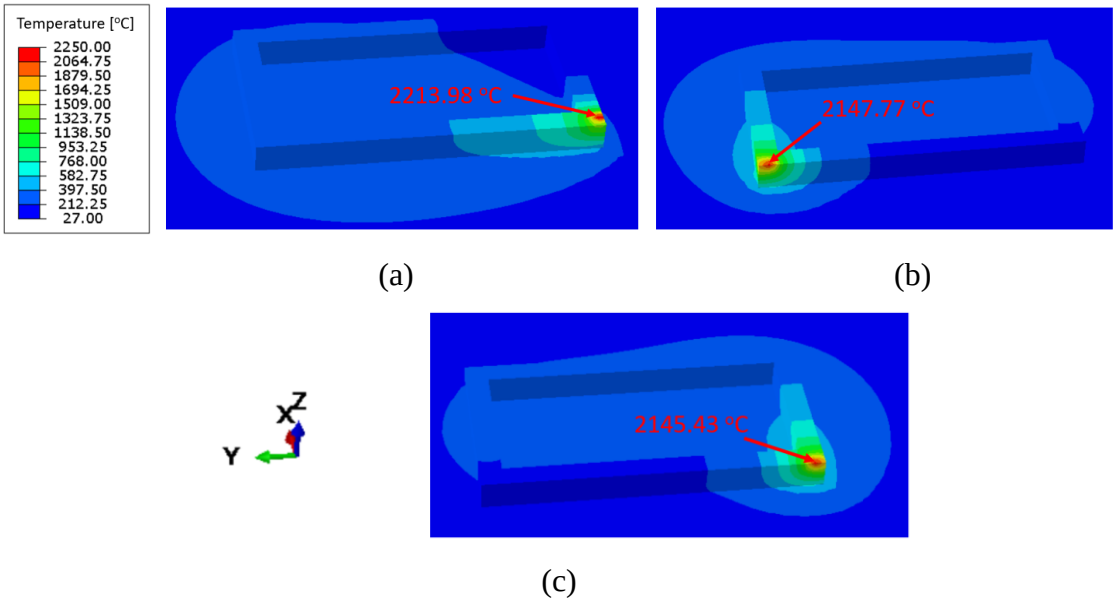

Fig. 16. The temperature contours at the end of layer 4 with different scanning strategies (see Fig. 7): (a) Strategy A, (b) Strategy B, (c) Strategy C.

3. 3 Residual stress of different scanning strategies

Fig. 17 shows the FE results of the final maximum principal stress distributions for the rectangular shaped Ti-6Al-4V specimens using the different scanning strategies. The scanning strategy (both laser scanning start point and direction) is seen to have a significant influence on the maximum principal stress distributions. Strategy B gives the highest maximum principal stress (818.6 MPa, Fig. 17 (b)) but a more uniform distribution when compared to the Strategy A, which gives the second highest maximum principal stress (780.5 MPa, Fig. 17 (a)), demonstrating the effect of changing the start point between each layer. Strategy C gives the lowest maximum principal stress (733.8 MPa, Fig. 17 (c)) indicating the beneficial effect of changing the laser direction between each layer, in terms of mitigating residual stress. Specifically, the model predicts about 12 % decrease of maximum principal stress in scanning strategy C compared to that of scanning strategy B.

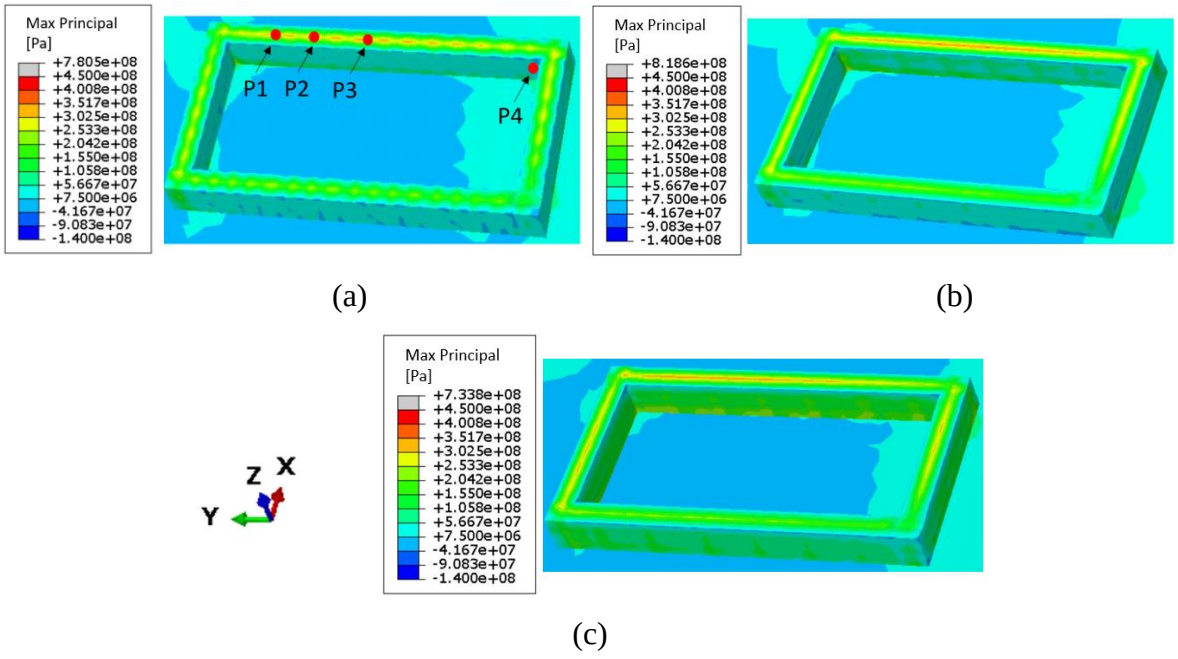

Fig. 17. The final maximum principal stress for different scanning strategies before releasing substrate constraints: (a) Strategy A, (b) Strategy B, (c) Strategy C.

Fig. 18 presents the predicted final σ_x residual stresses for the rectangular shaped Ti-6Al-4V specimens before releasing the substrate constraint, which shows that the σ_x stress on the

short side of rectangular shaped specimen is always higher than on the long side. Fig. 18 (a) shows that the highest σ_x stress (606.5 MPa) occurs with Strategy A (Fig. 7), which is 7 % larger than Strategy B (562.8 MPa, Fig. 18 (b)). Strategy C gives the lowest σ_x stress (528.5 MPa), as shown in Fig. 18 (c), which is 13 % lower than Strategy A. Strategies B and C have similar σ_x stress distributions and more uniform σ_x stress distribution on the longer side of the specimen than that of Strategy A.

Fig. 19 shows the σ_y residual stress distributions. Strategy B produces higher σ_y residual stresses (693 MPa, Fig. 19 (b)) than other two scanning strategies (Strategy A: 550.8 MPa, see Fig. 19 (a) and Strategy C: 595.3 MPa, see Fig. 19 (c)), which is different with the σ_x residual stress (Fig. 18). Strategy A is predicted with the lowest σ_y stress (550.8 MPa) but highest σ_x stress (606.5 MPa), which may be caused by higher temperature (Fig. 16). Except Strategy A, the other two scanning strategies have similar and more uniform σ_y stress distribution at the shorter side of the specimen.

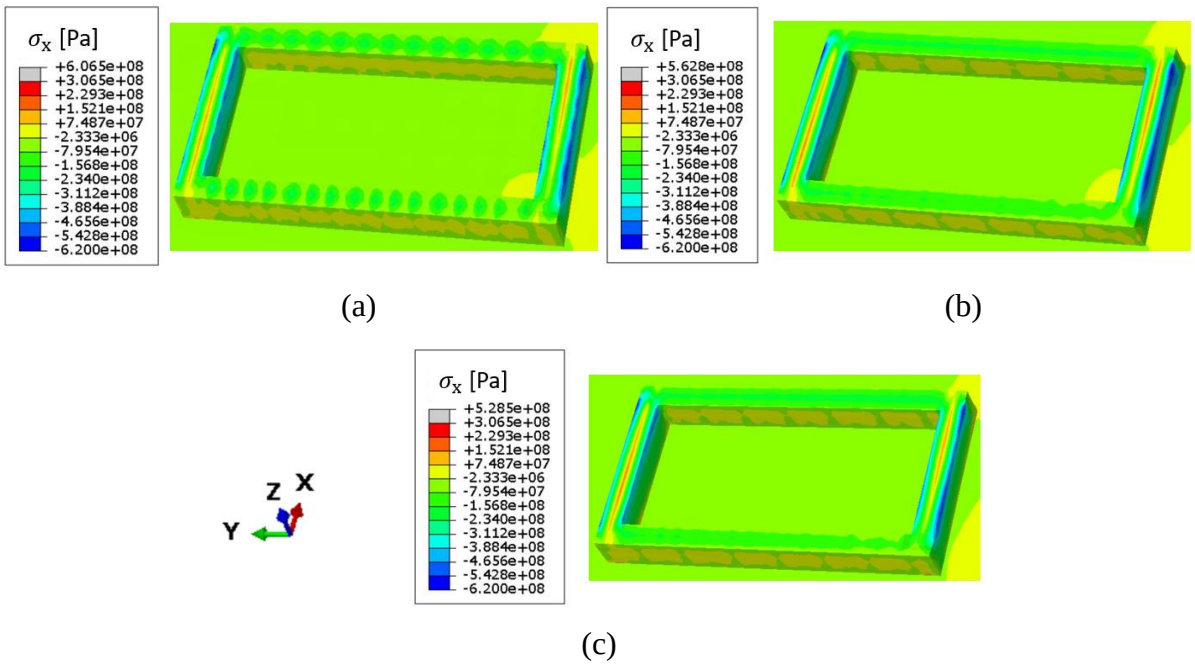

Fig. 18. The final σ_x residual stress distributions for different scanning strategies: (a) Strategy A, (b) Strategy B, (c) Strategy C.

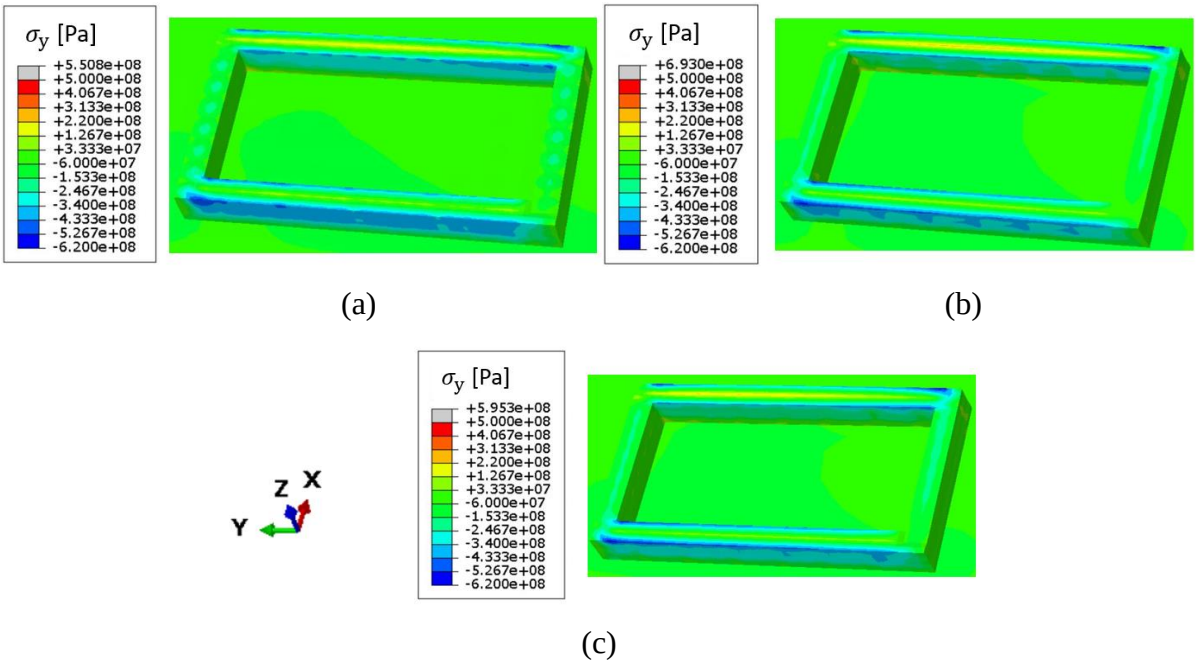

Fig. 19. The final σ_y residual stress distributions for different scanning strategies: (a) Strategy A, (b) Strategy B, (c) Strategy C.

Fig. 20 shows the comparison of predicted highest residual stress (σ_x, σ_y and maximum principal stress) for all the three scanning strategies (Fig. 7). The results of maximum principal stress and directional residual stress show that Strategy B gives the highest maximum principal and σ_y stresses, while the Strategy C gives the lowest maximum principal and σ_x stresses. Changing the laser direction between layers (Strategy C, Fig. 7) caused a 46.7 MPa lower maximum principal stress compared to keeping the same laser sequence for each layer (Strategy A, Fig. 7), which indicates that changing the laser direction between layers is beneficial for reducing residual stress.

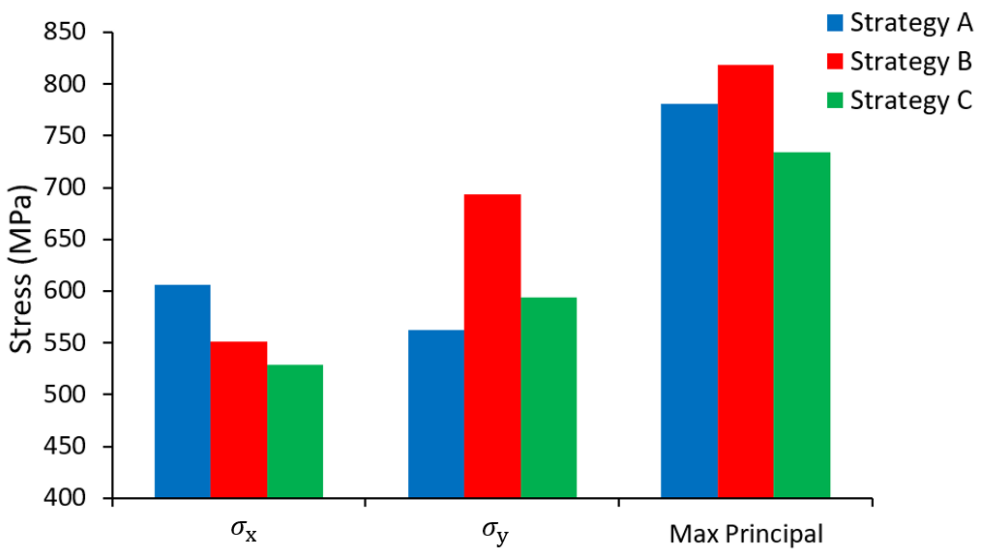

Fig. 20. Comparison of predicted maximum final residual stresses for different scanning strategies.

3. 4 Fatigue life prediction

The equation relating fatigue life N_f to stress range, mean stress and residual stress is given by combining the well-known Goodman equation for effect of mean stress with Basquin's equation [26, 27]:

$$N_f = \left[\frac{\sigma_a}{\sigma_f'\left(1 - \frac{\sigma_m + \sigma_r}{\sigma_{TS}}\right)}\right]^{\frac{1}{b}} \tag{14}$$

where σ_f' and b are high-cycle fatigue material constants, known as fatigue strength coefficient and exponent, respectively, σ_a is alternating stress range, σ_m is mean stress, σ_r is residual stress and σ_{TS} is ultimate tensile strength. The identified material constants and mechanical properties of as-built AM Ti-6Al-4V used in Eq (14) are provided in Table 4 [51, 52]. It is important to note that different AM process parameters can lead to different mechanical properties as the microstructures in the manufactured samples are different [53]. The alternating stress range and the mean stress are assumed to be 100 MPa and 200 MPa, respectively. Life predictions for four different sample locations, P1, P2, P3 and P4 (see Fig. 17 (a)) within the as-built AM Ti-6Al-4V component under Strategy A are given in Table 5. Table 6 shows the life predictions of as-built AM Ti-6Al-4V component at the location of maximum principal stress for each scanning strategy (Fig. 17).

Table 4. Identified material constants and mechanical properties of as-built AM Ti-6Al-4V [51, 52].

Fatigue strength coefficient σ_f' (MPa)	Fatigue strength exponent b	Ultimate tensile strength σ_{TS} (MPa)
1163	-0.046	1182

Table 5. Life predictions of as-built AM Ti-6Al-4V component at different positions under Strategy A (positions as labelled in Fig. 17 (a)).

	Position 1	Position 2	Position 3	Position 4
Residual stress σ_r (MPa)	650	700	750	-100
$\sigma_m + \sigma_r$ (MPa)	850	900	950	100
Basquin-Goodman N_f	1.50×10^{11}	4.32×10^{9}	6.20×10^{7}	2.14×10^{22}

Table 6. Life predictions of as-built AM Ti-6Al-4V component at the maximum principal stress position under different strategies.

	Strategy A	Strategy B	Strategy C
Residual stress σ_r (MPa)	780.5	818.6	733.8
$\sigma_m + \sigma_r$ (MPa)	980.5	1018.5	933.8
Basquin-Goodman N_f	2.90×10^{6}	3.04×10^{4}	2.69×10^{8}

4. Discussion

The present computational model offers an efficient and accurate method for simulation of the DED process of macro-scale metal components, which includes prediction of thermal histories during AM process and AM-induced residual stresses with effects of different scanning strategies. To the authors' knowledge, this is the first time the 'Abaqus AM' method has been presented for comparison against the layer-by-layer method (see Fig. 4) and investigation of effects of scanning strategies in DED process. Existing research usually focuses on one or two aspects with specific AM modelling techniques and AM process parameters, such as predicting residual stress with layer-by-layer method [14, 16], thermal analysis of DED process with different scanning strategies [54], thermal and mechanical behaviour prediction in the DED process using 'Model Change' technique [19, 32], which is

simulation complicated and computational costly.

In the thermal process simulation presented here, the layer-by-layer method is adopted to computationally predict the thermal history of the rectangular shaped Ti-6Al-4V specimen (Fig. 6) during DED process for simulation simplification and computational cost saving, however, the effect of scanning strategies cannot be investigated due to the physically realistic laser scanning path has been ignored [55] ((e.g. see Fig. 9). The new 'Abaqus AM' is employed to simulate the complete AM process (Fig. 5), and the generally-accepted double ellipsoidal volumetric Goldak heat source model (Fig. 3) is implemented via the built-in subroutine function to describe the heat flux during the DED process [38], in which the layer thickness is usually greater than that of PBF process [56], where the Gaussian surface heat flux is often used due to the minuscule layer thickness [21]. The predicted thermal history including peak temperatures and cooling rate, is validated by comparison with the published numerical and experimental results (see Fig. 10, Fig. 12) [19, 49]. It is clear that the model captures the peak temperatures reasonably well, but slightly over-predicts the cooling rates compared to the published numerical prediction (viz. ~ 200 ^{o}C/s, as compared to ~ 100 ^{o}C) (Table 3) [32]. However, the slight over-prediction by present model is within the typical cooling rate range (< 10^3 ^{o}C/s) [57], and is more close to the experimental measurement (219 $\pm$ 6.1 ^{o}C/s) from a five-layers Ti-6Al-4V DED process [48, 49]. The accuracy of present model could potentially be improved by including the typical physical phenomena, such as laser-powder interaction, phase transition (melting, vaporization and solidification), molten pool hydrodynamics [58, 59].

In the current mechanical process simulation, the sequentially coupled thermal and mechanical FE analysis strategy is employed due to the weak nature of mechanical to thermal field coupling in the DED process [24, 55]. It is worth pointing out that the fully coupled thermal-mechanical analysis, which takes much higher computational cost, has been compared to the sequentially coupled thermal-mechanical, where no significant difference is observed [19]. When the laser heating source starts along the x direction for depositing the shorter side for the first layer of the rectangular shaped Ti-6Al-4V specimen (Fig. 7), the compressive stress is generated for the material in front of the heating source due to thermal expansion, the tensile stress is generated in the deposition due to thermal contraction when the cooling starts after the heating source passes [28, 60]. The tensile (positive) σ_{x} residual stress which causes a bending shape deformation along the shorter side of the specimen when the part reaches at room temperature after the cooling period (see Fig. 14 (a)). The same analysis can be used for the

tensile σ_y residual stress along the y direction when the longer side of the specimen is being deposited (see Fig. 14 (b)). The predictions obtained from the present model are in reasonable agreement with the published numerical and experimental results [19, 32], providing confidence in the modelling approach.

Finally, the effect of scanning strategy on thermal profile and residual stress is investigated by defining different event series for simulating the laser beam movement path in Fig. 7. The present work managed to reveal and capture the impact of scanning strategy, which shows that the scanning strategy can determine both the temperature (Fig. 16) and stress distributions (Fig. 17, Fig. 18, Fig. 19) of the rectangular shaped Ti-6Al-4V specimen. Significant influence of the scanning strategy on the final part residual stress is also predicted by Zhang et.al. [37] and Lu et al. [47]. Woo et al. [61] experimentally measured residual stress of DED manufactured specimens with different strategies (bidirectional, orthogonal and island scan) by using four different methods (the contour method, neutron diffraction, and deep/incremental center hole drilling), demonstrating benefits of optimized residual stress distributions, as the range of stress values (changes from tension to compression) was significantly alleviated from 950 MPa for the bidirectional scan to 430 MPa for the island scan. The results obtained by different measurement methods are consistent. Table 5 shows that the increase of the tensile residual stress significantly decreased the fatigue life (see life predictions at positions from Position 1 to Position 3), and there will be a beneficial effect with the compressive residual stress (see life predictions at Position 4). Based on the results shown in Fig. 20 and Table 6, the appropriate scanning strategy should be considered for optimizing the residual stress of the specimen, particularly for mitigating tensile residual stresses, which is detrimental to the fatigue performance of AM parts [62].

A key next step for the present work, is the extension to include the effect of substrate constraints. Recently, Zhang et al. [37] have investigated the influence of substrate constraints on the residual stress, a decrease of around 200 MPa in maximum principal stress was found when comparing the predicted residual stress before and after releasing the substrate constraints.

The development of a process-structure-property (PSP) tool could make a significant contribution to the AM process optimization, such as saving time and cost compared to existing trial-and-error methods. Recently, Yang et al. [63] have presented a physically-based structure-property model for assessing the mechanical properties (yield stress, ultimate tensile strength, uniform elongation and flow stress) of PBF manufactured Ti-6Al-4V, including the effects of

solutes, grain size, phase volume fraction and dislocation density, the predicted tensile stress-strain responses are validated against measured tensile test data from 25 ^{o}C to 1000 ^{o}C. The effects of temperature-dependence on tensile stress-strain response is captured more accurately by including solid-state phase transformation (SSPT) effects, while stress is significantly over-predicted for temperatures above 400 ^{o}C when excluding the SSPT effects. In future work, it is planned to combine the current model with the process-structure model [21] for microstructure prediction based on the FE predicted thermal histories, and with the structure-property model [63] for resultant mechanical properties prediction of realistic, large-scale AM components, for capturing the effects of key AM manufacturing parameters for AM process optimization. Fatigue life prediction is particularly important for AM processed metals [64]. It is also intended to integrate the achieved PSP tool with our previously developed physically-based fatigue crack initiation (FCI) model [65] to predict effects of AM manufacturing process on the fatigue response of complex AM geometries, such as the conformal cooling injection moulding tools.

5. Conclusions

This paper presents a finite element modelling framework for the full process simulation of complex Ti-6Al-4V components in directed energy deposition additive manufacturing process. The method is based on the combined use of (i) application of the present FE-based AM method to define the additive manufacturing process parameters (moving heat source, toolpath, laser power, etc) as event series for input and (ii) the sequentially coupled thermo-mechanical analysis for the prediction of thermal profile and residual stress. The key conclusions are:

- The thermal and mechanical analysis are successfully validated against published numerical and experimental measurements, giving close agreement for temperature histories at different measurement locations. In particular, the new model shows significantly improved agreement of cooling rate, a key parameter for predicting phase transformations, with the measured result, compared to previously published simulations.
- Comparison with the more simplified, but commonly-used layer-by-layer method, with measured thermal histories and the proposed Abaqus AM method, has demonstrated that the layer-by-layer method is significantly less accurate for capturing peak

temperatures and specific temporal variation (e.g. cooling rate), particularly in relation to layer-based phenomena, as expected.

- The scanning strategy is shown to have a significant effect on temperature profile and residual stress of the rectangular shaped Ti-6Al-4V specimen during directed energy deposition. Changing laser direction between layers was shown to be beneficial for mitigating detrimental residual stress.
- Basquin-Goodman high cycle fatigue life calculations, for sample locations (residual stresses) within the as-built AM Ti-6Al-4V component, have demonstrated (i) the detrimental effects of AM-induced tensile residual stress, (ii) the beneficial effect of AM-induced compressive residual stress and (iii) the capability for mitigating detrimental residual stress effects via design of scanning strategy.
- The modelling results demonstrate the capability of the present FE-based AM method, which greatly reduces input-output data and computational time and makes the additive manufacturing process simulation of complex engineering components more feasible. Although this study focussed on the laser directed energy deposition process, the method is equally applicable to other AM processes, such as laser powder bed fusion process. Future work will focus on such processes.
- Further research work will require more accurate experimental measurements, such as the material constitutive behaviour and properties at elevated temperatures, to improve the accuracy of additive manufacturing process simulation.

Declaration of Competing Interest

The authors declare that they have no known competing financial interests or personal relationships that could have appeared to influence the work reported in this paper.

Acknowledgements

This publication has emanated from research conducted with the financial support of Science Foundation Ireland under Grant number SFI/16/RC/3872. For the purpose of Open Access, the author has applied a CC BY public copyright licence to any Author Accepted Manuscript version arising from this submission. J Zhou would also like to acknowledge helpful discussions with Dr. Wenyou Zhang and Dr. Noel Harrison, within the SFI I-Form Research Centre for Advanced Manufacturing in Ireland.

References

[1] M. Attaran, The rise of 3-D printing: The advantages of additive manufacturing over traditional manufacturing, Business Horizons, 60 (2017) 677-688.
[2] T. Gatsos, K.A. Elsayed, Y. Zhai, D.A. Lados, Review on Computational Modeling of Process–Microstructure–Property Relationships in Metal Additive Manufacturing, JOM, 72 (2020) 403-419.
[3] S.M. Thompson, L. Bian, N. Shamsaei, A. Yadollahi, An overview of Direct Laser Deposition for additive manufacturing; Part I: Transport phenomena, modeling and diagnostics, Additive Manufacturing, 8 (2015) 36-62.
[4] W.E. Frazier, Metal additive manufacturing: a review, Journal of Materials Engineering and performance, 23 (2014) 1917-1928.
[5] A. Vafadar, F. Guzzomi, A. Rassau, K. Hayward, Advances in metal additive manufacturing: a review of common processes, industrial applications, and current challenges, Applied Sciences, 11 (2021) 1213.
[6] B. Blakey-Milner, P. Gradl, G. Snedden, M. Brooks, J. Pitot, E. Lopez, M. Leary, F. Berto, A. du Plessis, Metal additive manufacturing in aerospace: A review, Materials & Design, (2021) 110008.
[7] D. Feenstra, R. Banerjee, H. Fraser, A. Huang, A. Molotnikov, N. Birbilis, Critical review of the state of the art in multi-material fabrication via directed energy deposition, Current Opinion in Solid State and Materials Science, 25 (2021) 100924.
[8] X. Song, S. Feih, W. Zhai, C.-N. Sun, F. Li, R. Maiti, J. Wei, Y. Yang, V. Oancea, L. Romano Brandt, A.M. Korsunsky, Advances in additive manufacturing process simulation: Residual stresses and distortion predictions in complex metallic components, Materials & Design, 193 (2020).
[9] E.R. Denlinger, J.C. Heigel, P. Michaleris, Residual stress and distortion modeling of electron beam direct manufacturing Ti-6Al-4V, Proceedings of the Institution of Mechanical Engineers, Part B: Journal of Engineering Manufacture, 229 (2015) 1803-1813.
[10] P.J. Withers, H. Bhadeshia, Residual stress. Part 1–measurement techniques, Materials science and Technology, 17 (2001) 355-365.
[11] P. Edwards, M. Ramulu, Fatigue performance evaluation of selective laser melted Ti–6Al–4V, Materials Science and Engineering: A, 598 (2014) 327-337.
[12] P. Edwards, A. O'conner, M. Ramulu, Electron beam additive manufacturing of titanium components: properties and performance, Journal of Manufacturing Science and Engineering, 135 (2013).
[13] M.F. Zaeh, G. Branner, Investigations on residual stresses and deformations in selective laser melting, Production Engineering, 4 (2010) 35-45.
[14] R.A. Barrett, T. Etienne, C. Duddy, N.M. Harrison, Residual stress prediction in a powder bed fusion manufactured Ti6Al4V hip stem, in, 2017.
[15] W. Zhang, M. Tong, N.M. Harrison, Resolution, energy and time dependency on layer scaling in finite element modelling of laser beam powder bed fusion additive manufacturing, Additive Manufacturing, 28 (2019) 610-620.
[16] C. Chen, S. Chang, J. Zhu, Z. Xiao, H. Zhu, X. Zeng, Residual stress of typical parts in laser powder bed fusion, Journal of Manufacturing Processes, 59 (2020) 621-628.
[17] K.S. Ribeiro, F.E. Mariani, R.T. Coelho, A study of different deposition strategies in direct energy deposition (DED) processes, Procedia Manufacturing, 48 (2020) 663-670.
[18] M. Rauch, U.V. Nwankpa, J.-Y. Hascoet, Investigation of deposition strategy on wire and arc additive manufacturing of aluminium components, Journal of Advanced Joining Processes, 4 (2021) 100074.
[19] Q. Yang, P. Zhang, L. Cheng, Z. Min, M. Chyu, A.C. To, Finite element modeling and validation of thermomechanical behavior of Ti-6Al-4V in directed energy deposition additive manufacturing, Additive Manufacturing, 12 (2016) 169-177.
[20] M. Chiumenti, E. Neiva, E. Salsi, M. Cervera, S. Badia, J. Moya, Z. Chen, C. Lee, C. Davies, Numerical modelling and experimental validation in Selective Laser Melting, Additive Manufacturing, 18 (2017) 171-185.

[21] X. Yang, R.A. Barrett, M. Tong, N.M. Harrison, S.B. Leen, Towards a process-structure model for Ti-6Al-4V during additive manufacturing, Journal of Manufacturing Processes, 61 (2021) 428-439.
[22] D. Systemes, Abaqus Analysis User's Guide 2018, Google Scholar, (2018).
[23] J.P. Pragana, I.M. Bragança, L. Reis, C.M. Silva, P.A. Martins, Formability of wire-arc deposited AISI 316L sheets for hybrid additive manufacturing applications, Proceedings of the Institution of Mechanical Engineers, Part L: Journal of Materials: Design and Applications, 235 (2021) 2839-2850.
[24] Y. Yang, M. Allen, T. London, V. Oancea, Residual Strain Predictions for a Powder Bed Fusion Inconel 625 Single Cantilever Part, Integrating Materials and Manufacturing Innovation, 8 (2019) 294-304.
[25] W. Jiang, X. Xie, T. Wang, X. Zhang, S.-T. Tu, J. Wang, X. Zhao, Fatigue life prediction of 316L stainless steel weld joint including the role of residual stress and its evolution: Experimental and modelling, International Journal of Fatigue, 143 (2021).
[26] R.J. Devaney, P.E. O'Donoghue, S.B. Leen, Global and local fatigue analysis of X100 and X60 steel catenary riser girth welds, Journal of Structural Integrity and Maintenance, 2 (2017) 181-189.
[27] C.A. Sweeney, P.E. McHugh, J.P. McGarry, S.B. Leen, Micromechanical methodology for fatigue in cardiovascular stents, International Journal of Fatigue, 44 (2012) 202-216.
[28] J. Ding, P. Colegrove, J. Mehnen, S. Ganguly, P.S. Almeida, F. Wang, S. Williams, Thermo-mechanical analysis of Wire and Arc Additive Layer Manufacturing process on large multi-layer parts, Computational Materials Science, 50 (2011) 3315-3322.
[29] F.E. Bock, J. Herrnring, M. Froend, J. Enz, N. Kashaev, B. Klusemann, Experimental and numerical thermo-mechanical analysis of wire-based laser metal deposition of Al-Mg alloys, Journal of Manufacturing Processes, 64 (2021) 982-995.
[30] L. Li, F. Liou, Numerical Investigation of Thermo-Mechanical Field during Selective Laser Melting Process with Experimental Validation, Metals, 11 (2021) 1003.
[31] M. Chiumenti, M. Cervera, N. Dialami, B. Wu, L. Jinwei, C.A. de Saracibar, Numerical modeling of the electron beam welding and its experimental validation, Finite Elements in Analysis and Design, 121 (2016) 118-133.
[32] C. Baykasoglu, O. Akyildiz, D. Candemir, Q. Yang, A.C. To, Predicting Microstructure Evolution During Directed Energy Deposition Additive Manufacturing of Ti-6Al-4V, Journal of Manufacturing Science and Engineering, 140 (2018).
[33] M. Chiumenti, M. Cervera, C.A. de Saracibar, N. Dialami, Numerical modeling of friction stir welding processes, Computer methods in applied mechanics and engineering, 254 (2013) 353-369.
[34] J. Heigel, P. Michaleris, E.W. Reutzel, Thermo-mechanical model development and validation of directed energy deposition additive manufacturing of Ti–6Al–4V, Additive manufacturing, 5 (2015) 9-19.
[35] M.F. Gouge, J.C. Heigel, P. Michaleris, T.A. Palmer, Modeling forced convection in the thermal simulation of laser cladding processes, The International Journal of Advanced Manufacturing Technology, 79 (2015) 307-320.
[36] S.A. Khairallah, A.T. Anderson, A. Rubenchik, W.E. King, Laser powder-bed fusion additive manufacturing: Physics of complex melt flow and formation mechanisms of pores, spatter, and denudation zones, Acta Materialia, 108 (2016) 36-45.
[37] W. Zhang, M. Tong, N.M. Harrison, Scanning strategies effect on temperature, residual stress and deformation by multi-laser beam powder bed fusion manufacturing, Additive Manufacturing, 36 (2020).
[38] J. Goldak, A. Chakravarti, M. Bibby, A new finite element model for welding heat sources, Metallurgical transactions B, 15 (1984) 299-305.
[39] C. Baykasoğlu, O. Akyildiz, M. Tunay, A.C. To, A process-microstructure finite element simulation framework for predicting phase transformations and microhardness for directed energy deposition of Ti6Al4V, Additive Manufacturing, 35 (2020).
[40] P. Michaleris, Modeling metal deposition in heat transfer analyses of additive manufacturing processes, Finite Elements in Analysis and Design, 86 (2014) 51-60.
[41] M. Chiumenti, M. Cervera, A. Salmi, C.A. De Saracibar, N. Dialami, K. Matsui, Finite element modeling of multi-pass welding and shaped metal deposition processes, Computer methods in applied

mechanics and engineering, 199 (2010) 2343-2359.
[42] B. Baufeld, O. van der Biest, Mechanical properties of Ti-6Al-4V specimens produced by shaped metal deposition, Sci Technol Adv Mater, 10 (2009) 015008.
[43] A. Anca, V.D. Fachinotti, G. Escobar‐Palafox, A. Cardona, Computational modelling of shaped metal deposition, International journal for numerical methods in engineering, 85 (2011) 84-106.
[44] E.R. Denlinger, J. Irwin, P. Michaleris, Thermomechanical modeling of additive manufacturing large parts, Journal of Manufacturing Science and Engineering, 136 (2014).
[45] M.F. Zaeh, G. Branner, Investigations on residual stresses and deformations in selective laser melting, Production Engineering, 4 (2009) 35-45.
[46] A.U. Manual, Abaqus user manual, Abacus, (2020).
[47] X. Lu, M. Cervera, M. Chiumenti, J. Li, X. Ji, G. Zhang, X. Lin, Modeling of the Effect of the Building Strategy on the Thermomechanical Response of Ti-6Al-4V Rectangular Parts Manufactured by Laser Directed Energy Deposition, Metals, 10 (2020).
[48] F. Lia, R. Martukanitz, J. Park, T. DebRoy, T. Mukherjee, J. Keist, S. Patankar, Process and microstructural validation of the laser-based directed energy deposition process for Ti-6Al-4V and Inconel 625 material, Process Microstruct. Valid. Laser-Based Dir. Energy Depos. Process Ti-6Al-4v Inconel, 625 (2015).
[49] F. Lia, J.Z. Park, J.S. Keist, S. Joshi, R.P. Martukanitz, Thermal and microstructural analysis of laser-based directed energy deposition for Ti-6Al-4V and Inconel 625 deposits, Materials Science and Engineering: A, 717 (2018) 1-10.
[50] S. Riza, S. Masood, C. Wen, Laser-assisted additive manufacturing for metallic biomedical scaffolds, (2014).
[51] D. Agius, K.I. Kourousis, C. Wallbrink, T. Song, Cyclic plasticity and microstructure of as-built SLM Ti-6Al-4V: The effect of build orientation, Materials Science and Engineering: A, 701 (2017) 85-100.
[52] R. Biswal, A.K. Syed, X. Zhang, Assessment of the effect of isolated porosity defects on the fatigue performance of additive manufactured titanium alloy, Additive Manufacturing, 23 (2018) 433-442.
[53] A. Sterling, N. Shamsaei, B. Torries, S.M. Thompson, Fatigue Behaviour of Additively Manufactured Ti-6Al-4V, Procedia Engineering, 133 (2015) 576-589.
[54] Y. Zhang, H. Jing, L. Xu, Y. Han, L. Zhao, Effects of different scanning patterns on nickel alloy-directed energy deposition based on thermal analysis, Virtual and Physical Prototyping, 16 (2021) S98-S115.
[55] R.J. Williams, C.M. Davies, P.A. Hooper, A pragmatic part scale model for residual stress and distortion prediction in powder bed fusion, Additive Manufacturing, 22 (2018) 416-425.
[56] Y. Zhang, L. Wu, X. Guo, S. Kane, Y. Deng, Y.-G. Jung, J.-H. Lee, J. Zhang, Additive manufacturing of metallic materials: a review, Journal of Materials Engineering and Performance, 27 (2018) 1-13.
[57] D. Herzog, V. Seyda, E. Wycisk, C. Emmelmann, Additive manufacturing of metals, Acta Materialia, 117 (2016) 371-392.
[58] J.I. Arrizubieta, A. Lamikiz, F. Klocke, S. Martínez, K. Arntz, E. Ukar, Evaluation of the relevance of melt pool dynamics in Laser Material Deposition process modeling, International Journal of Heat and Mass Transfer, 115 (2017) 80-91.
[59] A. Aggarwal, A. Chouhan, S. Patel, D. Yadav, A. Kumar, A. Vinod, K. Prashanth, N. Gurao, Role of impinging powder particles on melt pool hydrodynamics, thermal behaviour and microstructure in laser-assisted DED process: A particle-scale DEM–CFD–CA approach, International Journal of Heat and Mass Transfer, 158 (2020) 119989.
[60] J. Ding, Thermo-mechanical analysis of wire and arc additive manufacturing process, (2012).
[61] W. Woo, D.-K. Kim, E.J. Kingston, V. Luzin, F. Salvemini, M.R. Hill, Effect of interlayers and scanning strategies on through-thickness residual stress distributions in additive manufactured ferritic-austenitic steel structure, Materials Science and Engineering: A, 744 (2019) 618-629.
[62] N. Shamsaei, J. Simsiriwong, Fatigue behaviour of additively-manufactured metallic parts, Procedia Structural Integrity, 7 (2017) 3-10.
[63] X. Yang, R.A. Barrett, N.M. Harrison, S.B. Leen, A physically-based structure-property model

for additively manufactured Ti-6Al-4V, Materials & Design, 205 (2021).
[64] Z. Zhan, H. Li, K.Y. Lam, Development of a novel fatigue damage model with AM effects for life prediction of commonly-used alloys in aerospace, International Journal of Mechanical Sciences, 155 (2019) 110-124.
[65] J. Zhou, R.A. Barrett, S.B. Leen, A physically-based method for predicting high temperature fatigue crack initiation in P91 welded steel, International Journal of Fatigue, 153 (2021).